DEPLOYABLE BOOM FOR SUNSHIELD STRUCTURE OF LARGE SPACE TELESCOPE

Nailiang Cao[1,2*], Xiaohui Zhang[1], Zhilai Li[1], Fengwei Guan[1], Qinglei Zhao[1]

ABSTRACT: For less payload volume and better launch performance, the future large aperture space telescope must be designed on a lightweight, deployable sunshield structure. In this paper, a one-dimensional deployable boom is presented for large-aperture sunshield structure, aiming to satisfy the requirements on weight, stability and positioning. After creating a finite element model of the slit tube, the author applied displacement boundary condition on the one end and concentrated force on the other to obtain the distribution of stress and strain. Next, an 8m-long thin-walled slit tube was developed from carbon filter composite, and taken as a key component of deployable boom. The slit tube lays the basis for detailed design of the drive mechanism. The experiment shows that the deployable boom can move stably under an axial load of 30N, paving the way for the reliable deployment of sunshield structure.

KEY WORDS: Space Telescope, Deployable Sunshield Structure, Slit Tube, Deployable Boom.

1 INTRODUCTION

Sunshield structure, as an effective tool to improve imaging quality, has been widely used in remote sensing satellites to reflect sunlight and prevent stray light. The structure is a shared component of space optical payloads, including the SPOT series of satellites (France) (Zhang et al., 2014; Beckwith et al., 2006; Liu, 2016), the Hubble Space Telescope (US) (Li et al., 2009; Santiago-Prowald, 2015), and Gaofen-4 satellite (China) (Avrigean, 2015; Biris, 2016). However, the sunshield structures of these satellites are fixed and not extensible. With the widening of optical aperture, the traditional form of sunshield structure can no longer satisfy the dynamics requirements (Bataineh and Taamneh, 2017). All this gives rise to the research of deployable sunshield structure.

The deployable sunshield structure is an important branch of space deployable structure. Owing to the limited size of rocket, the structure is bound to proliferate in the future. In 2004, the US National Reconnaissance Office convened a meeting to discuss the concept of deployable telescope (Mohamed et al., 2017). The attendees planned to develop a reconnaissance satellite within two decades, which can pack into a 5m diameter rocket, and expand into a 30m diameter telescope after entering orbit (Blandeau et al., 2016). In the following year, the European Space Agency (ESA) made a clear proposal to create a deployable optical system for earth observation (Mukhopadhyay, 2016; Houria et al., 2017).

Nevertheless, there has not been any substantial progress in deployable sunshield structure, due to the huge investment and numerous technical difficulties (Alam, 2016). The existing projects on deployable sunshield structure include Prognoz warning satellites (Russia) (Kotova et al., 2005), James Webb Space Telescope (US) (Randy et al., 2016), SBIRS GEO satellite (US) (Andreas, 1997), Gaia satellites (Europe) (Wooldridge et al., 2000; Roman et al., 2010), MITAR satellite (Italy) (Roberto and Giulia, 2004; Giulia et al., 2004), the International X-ray Observatory (Robinson and Mcclelland, 2009), Astrium GO-3S satellites (Europe) (Jiang and Chen, 2012) etc. Not surprisingly, the structure has not been extensively explored in China. The few relevant studies include Jiang’s discussion over continuous deployable sunshield structure (Hou et al., 2002), and Guan’s design of an axially and radially deployable sunshield structure (Huang et al., 2015; Mackenzie et al., 2012)

Featuring a wide field of view, time-lapse fixed-point shooting and rapid response to emergencies, the geostationary high-resolution camera is of great help to develop a deployable sunshield structure. Recent years has seen heavy investment on geostationary high-resolution remote sensing in many countries. In light of the above, this paper presents a slit tube-based one-dimensional deployable boom for large-aperture sunshield structure.

[1] Changchun institute of Optics, Fine Mechanics and physics, Chinese Academy of Science, Changchun 130033, China
[2] University of Chinese Academy of Sciences, Beijing 100049, China
*Email: caonailiang@hotmail.com

2 ANALYSIS OF SUNSHIELD REQUIREMENTS

In the geostationary orbit, the satellite is static in relation to the earth. Thus, the heat flow of the satellite varies with the relative position of the sun and the earth. The typical working points of the satellite in orbit are the spring equinox, the summer solstice, the autumn equinox, the winter solstice. The heat flows at these four working points exhibit a dramatic seasonal change.

If the optical port of the camera is under direct sunlight, the heat will accumulate rapidly in the optimal satellite, resulting in a sharp increase of temperature and stray light. The length of the sunshield after deployment can be calculated with the formula below based on the minimum angle (8.7°) between the sunlight direction and the visual axis of the camera. This angle appears right at midnight.

$$L = \frac{D}{\tan\left(\theta + \frac{\varphi}{2}\right) - \tan\frac{\varphi}{2}}$$

(1)

where D is the camera's diameter; φ is the camera's field angle; L is sunshield length; θ is the angle between direct sunlight and the camera's optical axis.

According to the camera design, the camera's field angle is 0.64°, and the aperture diameter is 3m. Hence, the sunshield length should be 19.5m to avoid exposure to direct sunlight. For such a camera, the sunshield structure needs a one-dimensional axial folding function.

Based on the requirements on the full-scale and reduced-scale prototypes, the technical difficulties of the required sunshield structure were sorted out. To overcome these difficulties, the author analysed the preparation process, thermal stability, bearing characteristics, and drive mechanism based on thin-walled slit tube.

Table 1. Requirements on the full-size and reduced-scale prototypes

	Full-size prototype	Scale prototype
Expanded length	19.5 m	5.2m
Expansion ratio	1: 4	1: 4
Section size	φ180mm	φ110 mm
Stiffness index during launch	>45Hz	>50Hz
Stiffness index in orbit	>2Hz	>3Hz
Number of cycles	100 times	100 times
Surface treatment	Surface sprayed with high emissivity coating	

3 PREPARATION AND ANALYSIS OF THIN-WALLED SLIT TUBE

The required slit tube should have a thin-walled cylindrical structure. Depending on the number of components, the slit tube can be divided into monistic structure, dualistic structure and pluralistic structure. Each structure has its own cross-section pattern, namely open, lapped, interlocked, lensed, etc. (Table 2)

Similar to common tubes, the thin-walled slit tube has a cylindrical structure, except a gap on the bus of cylinder. The gap lowers the bending stiffness and torsional rigidity of slit tube. The torsional stiffness can be elevated by increasing the overlap. Besides, two thin-walls tubes can be adopted simultaneously to enhance bending stiffness and torsional rigidity. These properties of the double-tube mode can be further improved with the locking groove.

Table 2. Types of slit tube

	Monistic structure	Dualistic structure	Pluralistic structure
Open type	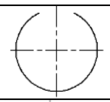		
Lap type	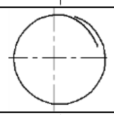	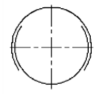	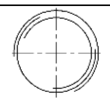
Interlock type	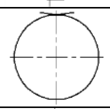	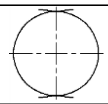	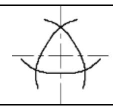
Lens type	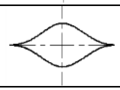	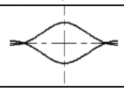	

3.1 Preparation of thin-walled slit tube

3.1.1 Material selection

The materials of the thin-walled slit tube were primarily selected based on strength and thermal properties. The material adaptability index can be expressed as follows:

$$\varepsilon = \frac{k\sigma_F}{CET * \alpha * E} \quad (2)$$

Where ε is the material adaptability index; k is the heat transfer coefficient; σ_F is the flattening stress; CET is the thermal expansion coefficient of the material; α is the surface absorption rate; E is the elastic modulus of the material. In most cases, the value of ε is proportional to the quality of the material.

Typical materials for the slit tube are beryllium copper alloy, carbon fibre composite, glass fibre composite, tungsten, molybdenum, etc. All of these materials boast high hardness and thermal conductivity (Table 3).

Table 3. Material properties

	Beryllium copper alloy	Carbon fiber	Glass fiber
Density (t/m^3)	8.1	1.6	2.4
Specific Stiffness	24.7	56.2	30.2
Thermal conductivity (mW/(mm℃))	83.7	35	45
Coefficient of thermal expansion (10^{-6}/℃)	18	0~3.2	2.7~7.2
Technology feasibility	good	better	bad
ε	34	89	21

According to the table above, the carbon fibre composite was selected as the slit tube material thanks to its suitable strength and thermal properties.

3.1.2 Preparation of carbon fibre thin-walled slit tube

As shown in Table 4, the main components of the carbon fibre composite include the M55J reinforcement material (high tensile strength and high tensile modulus), the matrix material of cyanate, and the J-133 adhesive material.

The specimen was prepared through a rather complicated process. The specific procedure involves winding, cutting, curing, grinding, stripping and inspection (Figure 1).

Table 4. Components of carbon fibre composite

Name	Grade	Performance	Use
Carbon fiber	M55J	Tensile strength 3500Mpa Tensile modulus 500GPa	Reinforced material
Cyanate	phenol-91		Matrix material
Adhesive	J-133	Tensile strength> 25MPa	Adhesive material

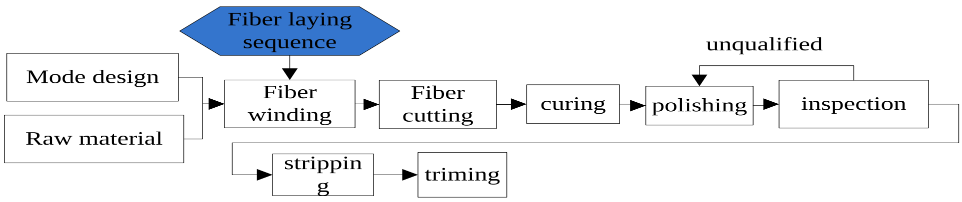

Figure 1. Preparation of carbon Fibre thin-walled slit Tube

Winding: Mount the core mold on the winding machine, and coat it with release agent; place the fibre on the mold in the pre-set sequence; tighten each layer with a tightening machine to remove the bubbles and impurities.

Cutting: Cut a slit on the tube with the cutting machine. This process must be completed before curing. Otherwise, the tube will collapse under internal elastic factors.

Curing: Place the workpiece into a sealed bag and vacuumize the bag; relocate the bag into a pressure vessel for curing; control the curing temperature in the following manner:

Room temperature~100℃: heat up at the rate of 1℃/min; vessel pressure<-0.1MPa;

100℃: maintain the temperature for 2h; vessel pressure <-0.1MPa;

100℃~120℃: heat up at the rate of 1℃/min; vessel pressure <-0.1MPa;

120℃: maintain the temperature for 2h; vessel pressure <-0.1MPa;

120℃: increase the pressure to 0.5MPa at the rate of 0.04MPa/min;

120℃: maintain the temperature for 2h; vessel pressure=0.5MPa;

120℃ ~90℃: cool down at the rate of 1℃/min; vessel pressure=0.5MPa;

90℃~ 50℃: cool down at the rate of 1℃/min and lower the pressure at the rate of 0.01MPa/min;

50℃: maintain the temperature for 0.5h; vessel pressure= atmospheric pressure;

Take the bag out of the vessel, and cool it down naturally to room temperature.

The curing process prevents the physical aging of the material and guarantees the thorough recrystallization of the composite material. The cured slit tube is deemed as stable and free of internal stress.

Grinding: Mount the cured product on the grinder, and polish its outer surface with abrasive paper. After grinding, the product should meet the requirements on the outer diameter and surface finish.

Stripping: Treat the product with special jigs in the stripping machine.

Inspection: Trim the thin-walled slit tube, and look for defects.

Through the above process, an 8m-long carbon fibre thin-walled slit tube was produced successfully (Figure 2).

Figure 2. 8m-long carbon fibre thin-walled slit tube

3.2 Stiffness analysis of slit tube

One of the most important features of a thin-walled slit tube is that the shear centre and centroid deviate from its geometric centre (Figure 3). Let us denote the deviation of shear centre from the geometric centre as Zs and the deivation of centroid from the geometric centre as Zc.

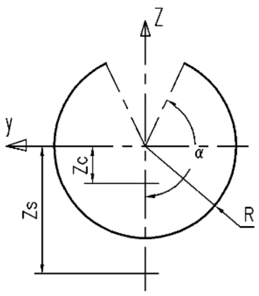

Figure 3. Cross-sectional drawing of slit tube

When an axial force is applied on the slit tube, there will be no additional torque if the tensile force passes through the centroid, and there will be additional bending moment or torque if otherwise (e.g. the tensile force passes through the geometric centre). In the latter case, the axial bearing capacity of the slit tube will plunge dramatically.

When a bending force is applied on the slit tube, there will be no torque if the bending force passes through the shear centre, and there will be a bending-torsional coupling if otherwise. Considering the low torsional rigidity of the thin-walled slit tube, the bearing capacity fluctuates violently with the position of bending force along the Y-direction:

$$\begin{cases} Z_c = \dfrac{R\sin\alpha}{\alpha} \\ Z_s = \dfrac{2R(\sin\alpha - \alpha\cos\alpha)}{\alpha - \sin\alpha\cos\alpha} \end{cases}$$

(3)

3.2.1 Analysis of bending stiffness

According to the analysis, the bending stiffness is lower in the Y direction than in the Z direction. Hence, the following analysis focuses on the case of a force exerted along the Y direction. The bending stiffness of the slit tube is calculated as:

$$EI = E_x R^3 t\left(\alpha + \sin\alpha\cos\alpha - \frac{2\sin^2\alpha}{\alpha}\right)$$

(4)

where EI is the bending stiffness; t is the thickness of the slit tube.

Bending stiffness is a major concern for engineering applications. Unlike the closed tube, the slit tube is prone to buckling failure under bending force. For the closed thin-walled tube, the buckling stress formula is:

$$\sigma_{cr} = \frac{E}{\sqrt{3(1-v^2)}}\frac{t}{R}$$

(5)

To extend the formula to the thin-walled slit tube, that the above formula is assumed to be valid:

$$\sigma_{cr} = \frac{kE}{\sqrt{3(1-v^2)}} \frac{t}{R} \quad (6)$$

where k is the correction factor of the opening angle α. k=1 for the closed tube, and k<1 for the slit tube.

The relationship between the opening angle α and k was determined based on finite element analysis and test data. As shown in Figure 4, the coefficient k is about 0.15 when the angle ranges between 330° and 360°. Moreover, the measured data are in good agreement with the results of the finite element analysis.

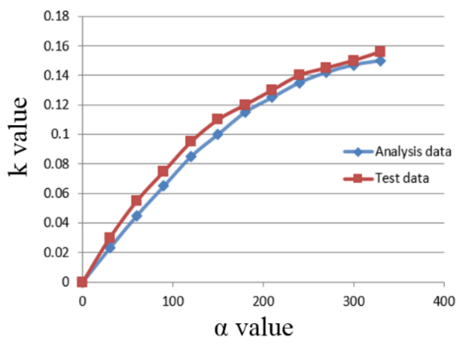

Figure 4. Relationship between the opening angle α and k

Based on the analysis data, the formula of coefficient k can be written as follows:

$$k = 0.33e^{\frac{\alpha}{2\pi}} \quad (7)$$

3.2.2 Finite element analysis

The ABAQUS software was employed to analyse the buckling of the slit tube under different loading directions. First, the thin-walled slit tube was fixed at one end and applied with a bending force along the Z direction at the other end. No additional torsional stress was observed due to the structural symmetry along the loading direction. Then, the finite element analysis was carried out to obtain the stress nephogram (Figure 5a). The maximum stress appeared near the fixed end. Further analysis shows that the buckling deformation occurred at the loading end first.

Then, the constraint condition was changed by fixing one end of the slit tube and applying a bending force in the Y direction at the other end. The force applied in the Y direction is different from that in the Z direction. An additional torque was observed because of the deviation of the bending force from the shear centre (Figure 5b). As can be seen from Figure 6b, the fixed end suffered from the buckling deformation first, and serious distortion appeared along the axial direction.

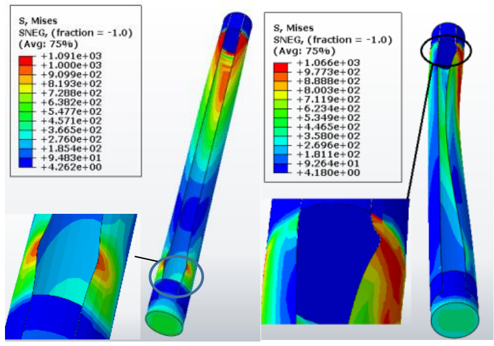

(a) (b)

Figure 5. Buckling of slit tube (a) in the Z direction (b) in the Y direction

For the initial cylindrical slit tube, assuming that the cylindrical axis is parallel to the X axis, then the initial state of the curvature matrix is:

$$\kappa_R = \begin{vmatrix} \kappa_x \\ \kappa_y \\ \kappa_{xy} \end{vmatrix} = \begin{vmatrix} 0 \\ \kappa_R \\ 0 \end{vmatrix} \quad (8)$$

where k_x and k_y are the bending curvature; k_{xy} is the tensile curvature.

Then, the author applied a force on the slit tube to produce deformation. Let us denote the resulting curvature as k_e and the shaft angle as θe. Then, the deformed curvature matrix is:

$$\kappa_e = \begin{vmatrix} \kappa_x \\ \kappa_y \\ \kappa_{xy} \end{vmatrix} = \kappa_e \begin{vmatrix} \sin^2 \theta_e \\ \cos^2 \theta_e \\ -2\sin\theta_e \cos\theta_e \end{vmatrix} \quad (9)$$

Thus, the change to curvature matrix is:

$$\kappa = \kappa_e - \kappa_R \quad (10)$$

Based on the classical laminar theory of composite materials, the strain matrix is:

$$\varepsilon^0 = \kappa A^{-1} B \quad (11)$$

where A is the tensile stiffness coefficient matrix related to the internal force and strain; D is the bending stiffness coefficient matrix related to the internal torque and the torque curvature; B is the coupling matrix between the tensile and the bending.

Therefore, the strain energy density of the laminate is:

$$u = \frac{1}{2}\left(\left(\varepsilon^{0}\right)^{T} A\varepsilon^{0} + 2\kappa^{T} B\varepsilon^{0} + \kappa^{T} D\kappa\right)$$
(12)

Based on formula (12), the strain energy distribution of the slit tube was obtained by finite element method (Figure 6).

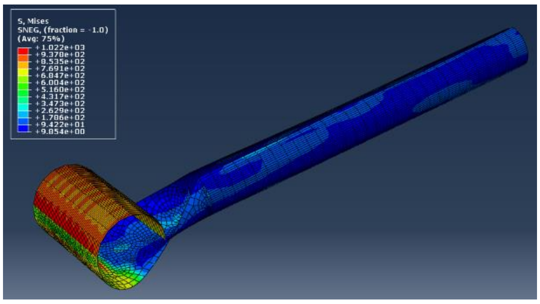

Figure 6. Strain energy distribution of the slit tube

4 DRIVING MECHANISM DESIGN OF DEPLOYABLE BOOM

There are three popular driving mechanisms of deployable boom, namely friction driving, belt driving, and gear driving. The friction driving relies on the rolling-wall friction of the slit tube. This mechanism has good adaptability as the drive force can be adjusted by the contact surface pressure, but does poorly in synchronization due to the stick-slip phenomenon. The belt driving operates on a steel strip of the same length with the slit tube. As the strip is retracted through motor, the slit tube stretches out under the force produced by the strip. So, this mechanism features good synchronization, and generates a driving force proportional to the torsional moment of the motor. The gear driving is realized by the smooth engagement/disengagement of gear teeth and tube hole. The downside of this mechanism is that the hole reduces the bending rigidity of the slit tube. Through the comparative analysis, the friction driving was selected as the driving mechanism in this research.

4.1 Driving mechanism analysis

The thin-walled slit tube was divided into three sections: the freedom section, the transition section and the folding section. In the freedom section, the tube segment is in cylindrical shape; this section has the maximum axial bearing capacity. In the transition section, the tube segment gradually shifts from the cylindrical state to the flatten state. In the folding section, the tube segment is flattened and coiled on a wheel; this section contains a large amount of strain energy. As shown in Figure 7, our driving mechanism is placed on the transition section.

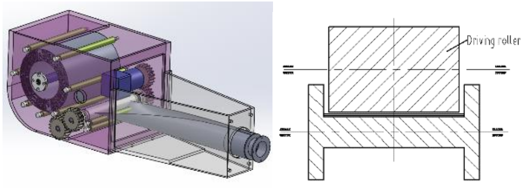

(a) (b)

Figure 7. Design of the deployable boom (a) Driving mechanism (b) Driving roller

5 PERFORMANCE TEST

The performance of the deployable boom was tested as follows. The examination of the driving force shows that: when the deployable boom stretched out under a certain load, the velocity fluctuated due to the difference between the dynamic and static friction coefficients (Figure 8a). Under the preload of 50N and the axial load of 15N, the velocity fluctuated by no more than 3%. The axial load surpassed the maximum bearing capacity of the mechanism when the velocity fluctuated beyond 10% of average velocity (Figure 8b). Dramatic velocity fluctuation was observed when the axial load increased to 45N.

Furthermore, it is discovered that the bearing capacity of the structure is proportional to the preload. However, the bearing capacity of the deployable boom vanished due to buckling when the preload surpassed a certain threshold.

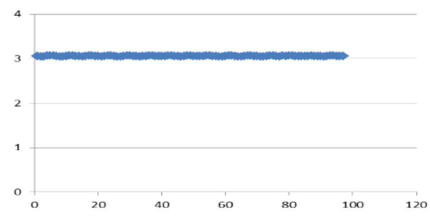

(a)

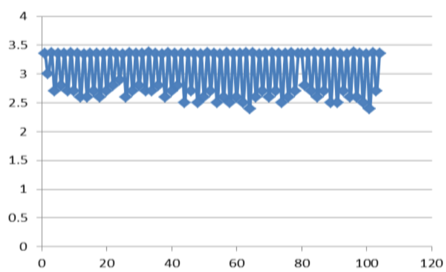

(b)

Figure 8. Velocity fluctuation (a) Preload is 50N and axial load is 15N (b) Preload is 50N and axial load is 45N

Our deployable sunshield structure consists of three deployable booms (Figure 9). During the deployment test of the structure, the three booms stretched out synchronously. Helium balloons were used to offload the gravity in the test.

The test results are satisfactory with smooth stretching-out and good speed consistency. Considering the high reliability requirements of deployable sunshield structure, the structure was also deployed in abnormal conditions (one of the three booms malfunctions). It is found that the structure can be deployed reliably with the driving force of the other two deployable booms.

Figure 9. Test with gravity offloading

6 CONCLUDING

For less payload volume and better launch performance, the future large aperture space telescope must be designed on a lightweight, deployable sunshield structure. In this paper, a one-dimensional deployable boom is presented for large-aperture sunshield structure, aiming to satisfy the requirements on weight, stability and positioning. Then detailed design of the deployable boom was completed based on the slit tube. The experiment shows that the deployable boom can move stably under an axial load of 30N, paving the way for the reliable deployment of sunshield structure.

7 ACKNOWLEDGEMENTS

This work is supported by the national key research and development program "static orbit high resolution light imaging camera system technology".

8 REFERENCES

►Alam, M. S. (2016). Mathematical modelling for the effects of thermophoresis and heat generation/absorption on MHD convective flow along an inclined stretching sheet in the presence of Dufour-Soret effects. Mathematical Modelling of Engineering Problems, 3(3), 119-128.

►Andreas, N. S. (1997). Space-Based Infrared System (SBIRS) system of systems. Aerospace Conference, Proc. IEEE, 429-438

►Avrigean, E. (2015). Optimization of the hub fork of a card an joint. Academic Journal of Manufacturing Engineering, 13(2), 66-71.

►Bataineh, K., Taamneh Y. (2017). Performance analysis of stand-alone solar dish Stirling system for electricity generation. International Journal of Heat and Technology, 35(1), 498-508.

►Beckwith, S. V., Ferguson, H. C., Lucas, R. A. (2006). The Hubble Ultra Deep Field. Astronomical Journal, 132(5), 1729-1755.

►Biriş, C. (2016). Considerations on manufacturing accuracy and surfacequality of nc laser cutting machine tools. Academic Journal of Manufacturing Engineering, 14(2), 33-39.

►Blandeau, M., Guerra, T. M., Pudlo, P., Gabrielli, F., Estrada-Manzo, V. (2016). Modelling seated postural stability for complete spine cord injury. Modelling, Measurement and Control C, 77(2), 40-50.

►Giulia, P., Luca, C. (2004). High resolution deployable telescope for satellite application. Proc. SPIE, 5234, 531-538.

►Hou, P. F., Ding, H. J., Guan, F. L. (2002). Circular crack in a transversely isotropic piezoelectric space under point forces and point charges. Acta Mechanica Sinica, 18(2), 159-169.

►Houria, H. S., Bariza, Z., Djamel, H., Hocine, B. (2017). DMFC water management in presence of heat sources. Mathematical Modelling of Engineering Problems, 4(1), 59-62.

►Huang, H., Guan, F. L., Tang, Y.S. (2015). Analysis of material performance test and reflection surface of inflatable ball antenna. Journal of Zhejiang University (Engineering Science), 2015, 49(4), 776-781.

►Jiang, F. M., Chen, F. S. (2012). Geosynchronous Orbit Follow-up can be Developed Special-shaped Hood Technology Research. Infrared Technology, 34(2), 73-77.

►Kotova, G., Verigin, M., Zastenker, G. (2005). Bow shock observations by Prognoz-Prognoz 11 data: analysis and model comparison. Advances in Space Research, 36(10), 1958-1963.

►Li, C., Wang, W., Fan, X. W. (2009). Advances in precision development of space telescope based on strip spring. China Optics and Applied Optics, 2(2), 85-90.

►Liu, H.Y. (2016). High score on the 4th launch of the "second five" aerospace mission satisfactorily ending. China Aerospace, (1), 20-20.

►Mackenzie, C., & Sweetman, B. (2012). Snakes And Lasers. Aviation Week & Space Technology, 174(23), 16-22.
►Mohamed, S., Mokhtar, A., Chatti, T. B. (2017). Numerical simulation of the compressible flow in convergent-divergent nozzle. International Journal of Heat and Technology, 35(1), 673-677.
►Mukhopadhyay N. (2016). Heat conduction model development of a cold storage using EPS insulation. Modelling, Measurement and Control B, 85(1), 18-27.
►Randy, A. K., Julie, M. (2016). Cryo-vacuum testing of the JWST Integrated Science Instrument Module. Proc. SPIE 9904, 408-420.
►Roberto, G., & Giulia, P. (2004). Realization and preliminary tests on an innovative deployable structure for a high resolution telescope for microsatellite. Proc. SPIE, 5570, 411-422.
►Robinson, D. W., McClelland, R. S. (2009). Mechanical Overview of the International X-Ray Observatory. Aerospace Conference. IEEE, 1-10.
►Roman, M., Hess, C., Cerqueira, R., et al. (2010). Gaia: A middleware infrastructure to enable active spaces. IEEE Pervasive Computing, 1(4), 74-83.
►Santiago-Prowald, J. (2008). Large Deployable Antenna Mechanical Concepts, CalTech Large Space Apertures Workshop, Pasadena, USA, 10-11.
►Wooldridge, M., Jennings, N. R., Kinny, D. (2000). The Gaia Methodology for Agent-Oriented Analysis and Design. Autonomous Agents and Multi-Agent Systems, 3(3), 285-312.
►Zhang, P, Lv, Z, Shi, W. (2014). Local Spectrum-Trend Similarity Approach for Detecting Land-Cover Change by Using SPOT-5 Satellite Images. IEEE Geoscience & Remote Sensing Letters, 11(4), 738-742.

.